# Monte Carlo Model of UV-Radiation Interaction with TiO$_2$-Coated Spheres

**Gustavo E. Imoberdorf, Orlando M. Alfano, Alberto E. Cassano, and Horacio A. Irazoqui**

INTEC, Instituto de Desarrollo Tecnológico para la Industria Química, Universidad Nacional del Litoral and CONICET, Güemes 3450, S3000GLM Santa Fe, Argentina

*Photocatalysis is one of the advanced oxidation techniques that are being studied for the treatment of polluted air and water from different sources. From a kinetic point of view, photocatalytic reaction rates are strongly dependent not only on the reactant and product concentrations, but also on the rate of photon absorption. Unfortunately, the local rate of photon absorption is usually difficult to evaluate because of (i) the inherent complexity of the system and (ii) the lack of data concerning the photocatalyst optical properties. The final objective of this project is focused on the development of a complete model of the radiation field; the bed structure, and the flow pattern to describe the operation of a fixed bed photocatalytic reactor. In this article, the interaction between radiative energy and TiO$_2$-coated fused-silica sphere beds was studied. The proposed model was built applying the Monte Carlo method, taking into account the complex reflection/refraction/absorption interactions between radiation and the packed bed. To obtain experimental measurements, an ad hoc device was designed and built. This device allows us to validate the proposed radiation model, and to obtain the optical parameters of the composite photocatalyst, i.e., the refractive index and the surface rough index of the fused-silica spheres, as well as the refractive index and the optical thickness of the TiO$_2$ films.* © 2007 American Institute of Chemical Engineers *AIChE J, 53: 2688–2703, 2007*
*Keywords: Monte Carlo, radiation, photocatalysis, modeling, sphere monolayer*

## Introduction

Photocatalytic reactions can be applied to reduce or eliminate most of gaseous effluents and waste water contaminants.[1–3] Several reactor configurations have been proposed to eliminate organic compounds from air[4–6] and water.[7,8] Most studies related to the photocatalytic degradation of gaseous pollutants were focused on the understanding of the reaction mechanisms; on the development of more active and stable photocatalysts; on the feasibility of the photocatalytic degradation of different pollutants; and on the development of more efficient reactor configurations. However, there are few publications specifically concerned to the design and scaling up of photocatalytic reactors.

A physical and mathematical model that simulates the performance of a photocatalytic reactor necessarily includes: a model of the momentum and mass transfer processes taking place in the fluid phase; a model of the radiation transfer processes occurring in the fluid phases and across the physical boundaries, as well as the intrinsic heterogeneous photocatalytic reaction kinetic expression. Particularly, the radiative energy transfer model is an essential component of photocatalytic reactor simulators, irrespective of their use for simulation, scale up or optimization purposes.[9]

Many configurations of photocatalytic reactors have been analyzed. Among the most attractive alternatives, we may include those reactors in which the photocatalyst is immobilized as thin films deposited on supporting fixed beds or on

the reactor walls, e.g., monolith reactors,[10–16] glass-fiber mesh reactor,[17] reticulated foam reactor,[18,19] corrugated plate reactor,[20–22] flat plate reactor,[23] multiannular reactor,[24–26] and annular packed-bed reactor.[27]

This work is a first step towards the full modeling, design, and construction of a photocatalytic annular fixed bed reactor. This reactor configuration has been realized in a way that the following goals can be achieved: high irradiated photocatalytic surface area; efficient radiative energy performance; low pressure drop; and reduced mass transfer resistances. The packing will consist of fused-silica spheres of non-negligible, uniform diameter, each covered with a $TiO_2$ film by means of a sol–gel technique. Fused-silica will be chosen as the supporting material on account of the negligible $SiO_2$ absorbance in the range of near UV wavelength (340–420 nm). The light source will be a black light and/or actinic UV lamp placed at the center of the reactor. The reactor cylindrical walls will be made of borosilicate glass tubes because of its high transmittance in the near UV region. The reactor dimensions, the UV lamp power, and all the rest of the design variables will be chosen in a subsequent step on the basis of model results.

The general methodology to model the photocatalytic fixed bed reactor broadly follows that proposed in a previous work.[28] The complete procedure was divided into three main steps. The first one consists in developing a radiative energy field model for a fixed bed, indispensable for obtaining the Local Superficial Rate of Photon Absorption (LSRPA) on the $TiO_2$ films, which are spatially distributed in the reactor packing. The optical properties and other parameters involved in this radiation model are also determined in this step. The second step consists in proposing and validating the kinetic expression of the photocatalytic degradation of a model gaseous pollutant. This kinetic expression should take into account the reaction rate dependence on the LSRPA, as well as on the concentration of reactants and products and on the catalyst loading. The experimentally measured reaction rate will be used to estimate the kinetic parameters of the proposed photocatalytic rate expression. The third step consists in using the radiation model, together with the kinetic model and the bed model, to solve the differential mass balance equation for the case of the photocatalytic fixed bed reactor. Regarding the bed model, the statistical model of a loose random packing proposed by Irazoqui et al.[29] will be adapted to our problem. The complete model will be used to single out the set of values of the relevant design parameters and operating variables that betters the reactor performance, according to different optimality criteria. Finally, the reactor will be built and operated, and the experimental results will be used to validate the proposed reactor model.

This work deals with the first stage mentioned before. Unfortunately, modeling the interaction between the radiation field and the catalytic bed in a photocatalytic fixed bed reactor is a difficult task to deal with, especially in those cases where the packing can not be simplified into a homogeneous pseudo-continuum. This situation arises when the size of the packing elements (for example, beads) is not negligible compared with the optical thickness of the bed. A statistical approach to this problem leads us to a structured (i.e., nonhomogeneous) pseudo-continuum medium. Most of the mathematical methods commonly used to evaluate the LVRPA can not be applied in structured continuum media.[18] Nevertheless, the Monte Carlo method is a valuable tool to solve the radiation transfer equation,[30–32] even in complex structured media.[18,19,33–36]

Monte Carlo modeling applied to solve the radiative energy transfer equation allows to predict the spatial distribution of the LVRPA (or the LSRPA) inside a photocatalytic reactor by taking into account the overall effect of a great number of photons whose trajectories are tracked individually. In this way, a complex problem is divided into simpler ones.[37] The trajectory of each photon can be tracked by using geometric optic laws, where the optical properties, such as absorbance or reflectance, are assimilated to the probabilities of the events they are associated with. Once every photon is tracked and the point of its probable absorption is defined, it is possible to calculate the spatial distribution of the rate of photon absorption inside the photocatalytic reactor. On the other hand, for validation purposes, it is also possible to evaluate the magnitude and direction of the radiation leaving the reactor. Another remarkable advantage of using the Monte Carlo method is that it can be implemented to sequentially solve a problem by combining and/or adding computational modules (submodels) that consider different physical phenomena or different events.

The objective of the present work is twofold: to propose and experimentally validate a Monte Carlo method developed to describe the radiation field in a simple packed bed (i.e., a monolayer of beads) that can be subsequently applied to the annular packed-bed photocatalytic reactor; and to obtain the optical parameters involved in this radiation model. The list of the radiative properties needed includes: the refractive index and the surface rough index of the bare fused-silica spheres, the refractive index of the fused-silica/$TiO_2$ coating composite and the optical thickness of the $TiO_2$ films. It is important to highlight that all the phenomena arising from the interaction between UV-radiation and a three-dimensional bed of spheres are already present in the case of the mono layer packing and they will be dealt with using the same techniques as those adopted and validated in the present work. Despite the obvious geometrical differences, beam reflection, attenuation and refraction occurring at the annular container walls in the three-dimensional case do not call for the inclusion of optical phenomena other than those already taken into account when considering the interaction between radiation and the mono layer supporting plate. The sequence of events that happen to a beam before either it fades out or leaves a multilayer bed will not include phenomena that have not been accounted for in the two-dimensional case, neither it will call for phenomenological parameters other than those regressed from the mono layer experiments.

In this stage, experiments are run in an ad hoc experimental setup (UV radiation emission–transmission-measuring apparatus or UV-RETM apparatus) designed to measure the flux of the energy transmitted in different directions through a monolayer of either $TiO_2$-coated or bare beads. The experiments are simulated with Monte Carlo techniques and the values of the radiative properties involved are those which give the best fit between experimental and simulated results. The radiation model takes into account the photon trajectory deflection due to refraction and reflection occurring at every point where a beam intercepts a sphere, as well as the UV
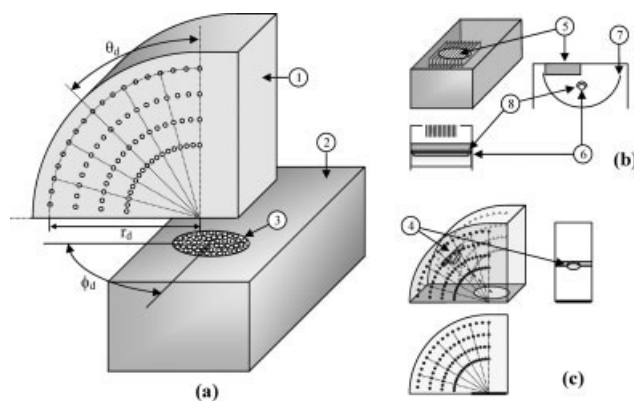
**Figure 1. Experimental setup: (a) sketch of the UV-RETM apparatus; (b) radiation emitting system; (c) measuring device.**

Keys: (1) measuring device, (2) emitting system, (3) glass plate, (4) radiometer, (5) screen of blackened plates, (6) UV lamp, (7) parabolic mirror, (8) blackened half-cylinder.

absorption in the TiO$_2$ film and the radiative exchange between spheres. To accomplish this, the ray-tracing method, the Snell and Fresnel equations, the Gauss rough surface model, and a monolayer model were used.

## Experimental

### Experimental setup

The UV-RETM apparatus (Figure 1a) was designed and built to study the interaction between a UV radiation field and a monolayer of either bare or TiO$_2$-coated spherical beads. This device comprises of two components, namely a radiation source of vertically-oriented UV rays (Figure 1b) and a measuring device (Figure 1c). Interposed in the way of the rays going from their source to the detector, a monolayer of spheres made of fused-silica, either bare or coated with a TiO$_2$ film, is held on a borosilicate glass plate (transparent to the employed useful radiation).

The radiation source consists of a tubular UV lamp (Philips TLD 18W/08 F4T5/BLB), of 1.4 cm diameter and 59 cm long with 3.5 W output power, aligned with the focal line of a cylindrical parabolic mirror. To prevent the direct radiation from reaching the glass plate, the upper longitudinal half of the cylindrical lamp surface is covered by a blackened half-cylinder sheet. The lamp diameter is small compared with the distance from the lamp axis to the vertex of the parabola. Under these conditions, the reflected rays will approximately lie on vertical planes parallel to the longitudinal symmetry plane of the mirror. Nevertheless, reflected rays will hardly lie on the mirror cross sections, but will have linear trajectories tilted in the longitudinal direction. To eliminate those rays with directions that differ from the vertical by an angle larger than an acceptable experimental error, a screen of blackened rectangular fins assembled vertically in a parallel arrangement (7 cm height, separated 0.7 cm from each other), was mounted on top of the radiation source setup as sketched in Figure 1b. Those rays too tilted to be considered vertically-oriented are absorbed on this screen. Although the radiation source setup emits UV rays with a

direction almost normal to the plate, the actual directions of the vertically-oriented rays were considered when processing experimental data.

A horizontal borosilicate glass plate is arranged above the radiation emitting system. It supports a uniformly distributed single layer of fused-silica beads. The average number of beads per unit area is chosen so that the fraction of solids, taken at one-bead radius distance from the glass plate, equals the corresponding value in a loose random packing, as discussed elsewhere.[29]

The experimental setup is completed with the radiation measuring device (Figure 1c) that consists of a UV-radiometer mounted on a support that allows to aim the detector at different directions. The vertically-oriented rays emitted by the radiation source are partially transmitted through the glass plate and scattered by the layer of fused-silica beads in different directions. All possible scattering directions are surveyed with the UV-radiometer (International Light IL 1700 SED005/WBS320/W, sensitive to radiation in the 300–420-nm interval), and the local net radiation flux is measured. The detector was held at different positions ($\phi_d$, $\theta_d$, $r_d$), and it was aimed at the center of the circular monolayer of beads on the glass plate, as shown in Figure 1c.

### Experimental procedure

Local net radiation flux measurements were made under four different conditions: (i) with the detector directly placed on the glass plate, without beads spread on it; (ii) with the detector at different ($\phi_d$, $\theta_d$, $r_d$) positions without beads on the glass plate; (iii) with the glass plate supporting a monolayer of bare fused-silica beads and the detector at different ($\phi_d$, $\theta_d$, $r_d$) positions, and (iv) with the glass plate supporting a single layer of fused-silica beads coated with a TiO$_2$ film and the detector at different ($\phi_d$, $\theta_d$, $r_d$) positions. In cases (iii) and (iv), a uniform distribution of beads in the monolayer was obtained by spreading at random a given mass of dry fused-silica beads (either TiO$_2$-coated or bare) and then vibrating the preliminary arrangement so that any eventual bead superposition could be eliminated. In cases (ii)–(iv), the readings were made by placing the radiometer at different $\theta_d$ (i.e., $\theta_d = 0°$, $5°$, $10°$,..., $85°$) and different $\phi_d$ angles (i.e., $\phi_d = 0°$, $45°$, $90°$,..., $315°$). Because of the symmetry of the problem, the single and higher order particle distribution functions must remain invariant under arbitrary rotations around the normal to the plate at the center point of the circular layer (i.e., these distributions must be $\phi_d$-invariant regardless the number of particles in the different subsets whose distribution they represent). We are interested on $\phi_d$-averaged readings at constant $\theta_d$, thus ironing out naturally occurring fluctuations around the average. The average readings of the incident radiation on the detector are invariant under such rotations. By contrast, the radiometer readings are strongly dependent on the polar angle ($\theta_d$). By considering the azimuthal symmetry of the measurements, $\phi_d$-averaged values corresponding to each $\theta_d$ angle were obtained.

### Catalyst preparation

The catalyst employed was TiO$_2$ deposited on fused-silica spheres (0.1 cm diameter) as a coating thin film. A sol–gel

technique[38] was used to fix the $TiO_2$ on the spheres. A volume of 415 cm³ of triple-distilled water was mixed with 4.5 cm³ of concentrated nitric acid (Anedra, 65%). Then, 35 cm³ of titanium isopropoxide (Aldrich, 97%) solution were added to this mixture and peptized under stirring during 10 h at 80°C until a clear sol was obtained. The fused-silica spheres were submerged in the titania sol and then the liquid in excess was drained. Then, the catalyst was dried in an oven at 80°C, and this coating process was repeated once again. Finally, the $TiO_2$-coated spheres were calcined at 200°C during 6 h.

## Model Development

Our final objective is modeling a photocatalytic fixed bed reactor. However, this objective is difficult to achieve in just one step because of the complexity of the system and the lack reported values of both, the optical properties involved and the photocatalytic kinetic models. In this work, the interaction between UV radiation and the simplest among the possible sphere beds, consisting of a bead monolayer is thoroughly studied.

Although the complete modeling of the photocatalytic reactor was divided into simpler steps, the modeling of the interaction between the UV radiation and the monolayer brings into play every physical event that occurs in the more complex, three-dimensional bed. The developed model of the radiation field is based on the assumption that any beam can be affected by the events sketched in Figure 2 in terms of beam trajectories; i.e.:

• As an emitted beam travels through the monolayer, it can be intercepted by any of the spheres (event 1) or not (event 2).

• The beam intercepted by a sphere (event 1) will be partially reflected (event 3) and partially refracted (event 4) by the air–silica rough interface.

• When a beam trajectory intercepts a $TiO_2$-coated sphere, that beam will be partially attenuated by the $TiO_2$ film and partially refracted (event 4)

• If a beam has been intercepted by a sphere and also has been refracted by the air/fused-silica rough interface (event 4), it will enter the sphere, then it will propagate through the fused-silica bulk, and finally reach the fused-silica/air rough interface (event 5). At this point, the beam will be partially refracted (event 6) into the gas phase and partially reflected back into the silica bulk phase (event 7). The latter of these events (event 7) will cause multiple reflection-and-refraction events (event 8) until the beam reflected back into the bulk has lost most of its energy through repeated leaks to the gas phase caused by successive refractions (event 9).

• Besides, the beam leaving a sphere can be intercepted by another sphere, causing radiative exchange between them (event 9).

• If any beam is intercepted by the glass plate (event 10), it will be partially refracted (event 11) and partially reflected (event 12).

• A given bean can be affected by several of the events just mentioned, until it leaves the monolayer.

This series of coupled events were modeled using Monte Carlo techniques. To obtain the parameters and the optical properties involved in the complete model from experimental results, a four-step strategy has been followed.

*Characterization of the radiation generated by the emitting system:* To interpret properly the experimental results obtained with the UV-RETM apparatus, it was necessary to characterize the radiation leaving the glass plate. In this subsection, the averaged value of the net radiation flux on the glass plate, the spectral composition of the UV radiation, and the directional dependence of the emitted radiation energy were determined.

*Beads monolayer simulation:* Modeling of the radiation field in a structured medium requires knowing the pattern of such structures. In this subsection a simple procedure developed to simulate the complete set of positions of each sphere on the monolayer is explained.

*Interaction between radiation and uncoated fused-silica spherical beads:* Experimental measurements were done employing an uncoated monolayer of spheres. The values obtained were analyzed by means of a complete radiation model to estimate the required properties of the fused-silica spheres, namely the refractive index and the surface roughness index.

*Interaction between radiation and $TiO_2$-coated fused-silica spherical beads:* This step is aimed at obtaining the optical thickness and the effective refraction index of the $TiO_2$ films. For this, measurements were done on a monolayer of $TiO_2$-coated spheres.

Before discussing the mathematical models in detail, it is convenient to define the coordinate systems that will be used in the coming sections. Two complementary coordinate systems will be used, namely a main coordinate system and an auxiliary frame. The main coordinate system (Figure 3a) has its origin at the center of the circular glass plate. A position referred to the coordinate system will be expressed either in terms of rectangular ($x_p$, $y_p$, $z_p$) or spherical ($r_p$, $\theta_p$, $\phi_p$) coordinates. This coordinate system will be used to define the spheres and detector locations and the trajectories of photons. The auxiliary coordinate system (Figure 3b) is centered at a particular point ($x_{0,p}$, $y_{0,p}$, $z_{0,p}$) on the circular glass plate. This coordinate system will be used only to indicate the motion direction of a given photon, and will be expressed in terms of spherical coordinates ($r_0$, $\theta_0$, $\phi_0$).
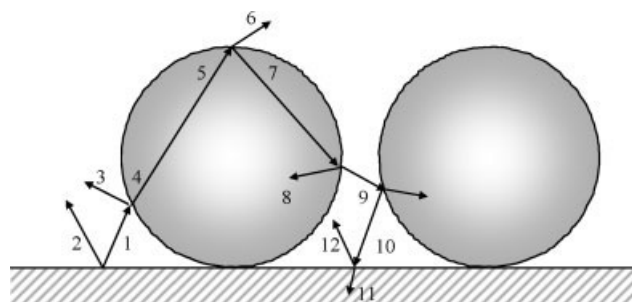


**Figure 2. Schematic representation of the possible interaction events between radiation and a bed of spheres.**
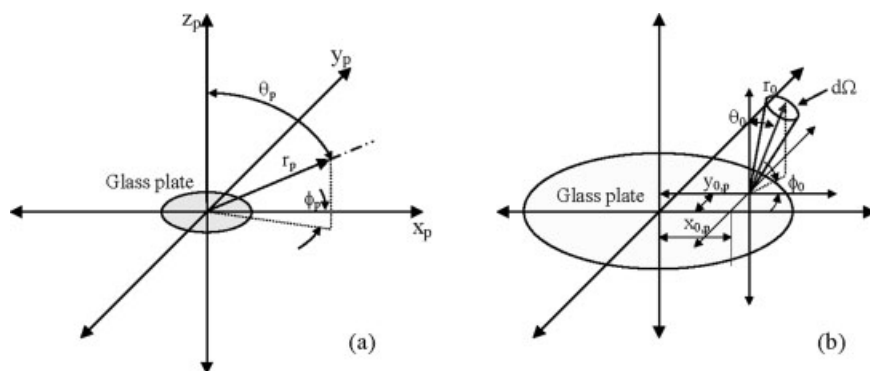
**Figure 3. Coordinate systems: (a) main coordinate system, (b) auxiliary coordinate system.**

The local net spectral radiation flux $q_\lambda(\mathbf{x})$, at the position $\mathbf{x} = (x_p, y_p, z_p,)$, is defined as follows:

$$q_\lambda(\mathbf{x}) = \int_\Omega I_\lambda(\mathbf{x}, \mathbf{\Omega}) \mathbf{\Omega} \cdot \mathbf{n}_{gp} d\Omega$$

$$= \int_{\theta_0=0}^{\pi/2} \int_{\phi_0=0}^{2\pi} I_\lambda(x_p, y_p, z_p, \phi_0, \theta_0,) \sin\theta_0 \cos\theta_0 \, d\phi_0 \, d\theta_0 \tag{1}$$

where $I_\lambda(\mathbf{x}, \mathbf{\Omega})$ is the spectral specific radiation intensity associated with the energy of the beams leaving the flat plate at $\mathbf{x}$ with direction $\mathbf{\Omega} = \mathbf{\Omega}(\theta_0, \phi_0, 1)$; $\mathbf{n}_{gp}$ is the upwardly directed unit vector normal to the glass plate, and $d\Omega = \sin\theta_0 d\phi_0 d\theta_0$ is a differential solid angle around the direction $\mathbf{\Omega}$.

The local net radiation flux is defined as:

$$q(\mathbf{x}) = \int_{\lambda_{min}}^{\lambda_{max}} q_\lambda(\mathbf{x})d\lambda = \sum_{\lambda_{min}}^{\lambda_{max}} q_\lambda(\mathbf{x}) \tag{2}$$

Finally, we define the surface coverage degree of the glass plate by the monolayer of spheres as the ratio of the spheres projected area to the glass plate area:

$$\eta_{g\text{-}p} = n_{sp} \left( \frac{r_{sp}}{r_{g\text{-}p}} \right)^2 \times 100 \tag{3}$$

where $n_{sp}$ is the total number of spheres located on the glass plate, $r_{g\text{-}p}$ is the glass plate radius ($r_{g\text{-}p}$ = 4 cm), and $r_{sp}$ is the sphere radius ($r_{sp}$ = 0.05 cm).

In the following subsections, a detailed description of the four steps involved in the complete modeling and in the optical parameters determination is presented.

### Characterization of the radiation generated by the emitting system

Knowing the characteristics of the UV radiation generated by the emitting system is essential to accurately analyze the values of the local net radiation flux measured with the radiometer. The required information is: (i) the average value of the net radiation flux on the glass plate, (ii) the spectral distribution of the UV radiation, and (iii) the dependence of the

emitted radiative energy on its direction of propagation. In this subsection, details of the procedure we followed to obtain this information are given.

(i) *Average value of the net radiation flux on the glass plate:* Because of the emitting system configuration, the local net radiation flux is assumed to be almost uniform on the glass plate surface. The average value of the net radiation flux on the glass plate is given by:

$$\left\langle q_{z_p=0}(x_p, y_p) \right\rangle_{A_{g\text{-}p}} = \left\langle q_{\theta_p=\frac{\pi}{2}}(r_p, \phi_p) \right\rangle_{A_{g\text{-}p}}$$

$$= \frac{\int_{\phi_p=0}^{2\pi} \int_{r_p=0}^{r_{g\text{-}p}} q_{\theta_p=\frac{\pi}{2}}(r_p, \phi_p) r_p dr_p d\phi_p}{\int_{\phi_p=0}^{2\pi} \int_{r_p=0}^{r_{g\text{-}p}} r_p \, dr_p d\phi_p} \tag{4}$$

where $A_{g\text{-}p}$ is the surface area of the glass plate and $q_{z_p=0}(x_p, y_p)$ is the local net radiation flux at the $(x_p, y_p)$ position on the $A_{g\text{-}p}$ surface.

To obtain experimental values of the local net radiation flux, the UV radiometer was placed at different positions directly on the glass plate surface. The average value has been determined by calculating the mean value of these experimental measurements:

$$\left\langle q_{z_p=0}(x_p, y_p) \right\rangle_{A_{g\text{-}p,exp}} = \frac{\sum_{i=1}^{n_m} q_{z_p=0,exp}(x_{p,i}, y_{p,i})}{n_m} \tag{5}$$

where $q_{z_p=0,exp}(x_{p,i}, y_{p,i})$ is the $i^{th}$ value of the local net radiation flux measured and $n_m$ is the total number of measurements. The value of the average net radiation flux on the glass plate is

$$\left\langle q_{z_p=0}(x_p, y_p) \right\rangle_{A_{g\text{-}p,exp}} = 5.635 \times 10^{-5} \text{ W cm}^{-2} \tag{6}$$

(ii) *Spectral distribution of the UV radiation:* The spectral distribution of the power emission of the UV lamp was obtained from the technical specifications catalog provided by the manufacturer. The spectral power of the UV lamp will be particularly useful for modeling when considering spectral properties, as it is the case of $TiO_2$ absorption coefficient.

(iii) *Propagation direction dependence of the local net radiation flux on the glass plate:* Although the radiation

source setup was designed to emit UV rays with direction as close as possible to the normal to the glass plate, the emitted rays are not completely vertical because of the aberration effects on the radiation source. Consequently, it is necessary to take into account the actual directions of the rays when processing experimental data.

To determine a propagation direction distribution function of the local net radiation flux on the glass plate, experimental values were obtained. This set of experimental data were gathered using the radiation measuring device, but without spheres on the glass plate. As is shown in Figure 4a, the UV radiometer was placed at different angles ($\theta_d$, $\phi_d$), located at the same distance from the center of the glass plate ($r_d = 30$ cm). The readings were made at different $\theta_d$ (i.e., at $\theta_d = 0°, 5°, 10°, \ldots, 85°$), and different $\phi_d$ (i.e., at $\phi_d = 0°, 45°, 90°, \ldots, 315°$). As expected, the measured values of the local net radiation flux show a strong dependence on the $\theta_d$ angle: high values of $q_{r_p=r_d}(\theta_d, \phi_d)$ are obtained when $\theta_d$ is close to zero, but negligible values are obtained when $\theta_d$ is higher than $15°$. On the contrary, the measured values of the local net radiation flux show a very small dependence on the $\phi_d$ angle (due to rotational symmetry).
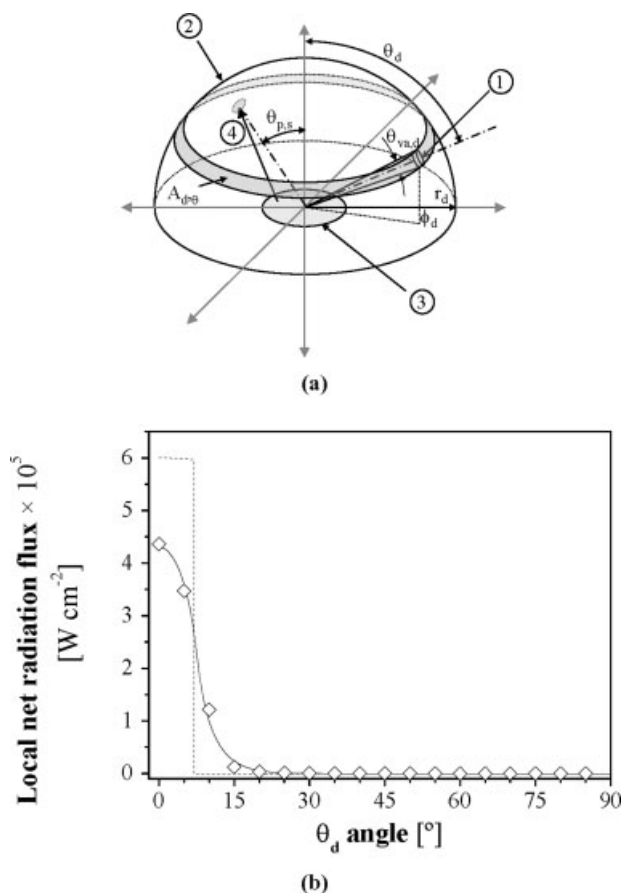


(a)



(b)

**Figure 4. (a) Relative position of the UV detector and (b) local net radiation flux against $\theta_d$ angle.**

Keys for (a): (1) UV radiometer, (2) hemispherical area where the detector can be placed, (3) plane plate, (4) outgoing beam. Keys for (b): ($\diamondsuit$) experimental values, (····) predicted values assuming parallel beams, (—) predicted values assuming non-parallel beams.

Consequently, $\phi_d$-averaged experimental values of the net radiation flux were obtained for different $\theta_d$ angles:

$$\langle q_{r_p=r_d}(\theta_d, \phi_d)\rangle_{\phi,\exp} = \frac{\sum_{i=1}^{n_m} q_{r_p=r_d}(\theta_d, \phi_{d,i})}{n_m};$$
$$\theta_d = 0°, 5°, 10°, \ldots, 85° \quad (7)$$

where $n_m$ is the number of experimental readings of the net radiation flux corresponding to each $\phi_d$ value. Figure 4b shows the experimental values of $\langle q_{r_p=r_d}(\theta_p, \phi_p)\rangle_{\phi,\exp}$ against the $\theta_d$ angle ($\diamondsuit$ symbols).

The experimental values of $q_{r_p=r_d}(\theta_d, \phi_d)$ are compared with the local net radiation flux values calculated when considering the emitted radiation as parallel rays normal to the glass plate. From a statistic point of view, the parallel rays hypothesis is equivalent to assume that the probability function that a given photon leaves the glass plate with a $\theta_0$ angle is

$$P(\theta_0) = \delta(\theta_0) \quad (8)$$

where $\delta(\cdot)$ is the Dirac delta function. In other words, Eq. 8 means that all the emitted beams will have the same direction, normal to the glass plate ($\theta_0 = 0$). The local net radiation flux at the radiometer position due to parallel rays is given by:

$$\langle q_{r_p=r_d}(\theta_d, \phi_d)\rangle_{\phi,\text{p-r}}$$
$$= \langle q_{z_p=0}(x_p, y_p)\rangle_{A_{g-p}} H\left(\sin^{-1}\left(\frac{r_{g-p}}{r_d}\right) - \theta_d\right) \cos\theta_d \quad (9)$$

where $H(\cdot)$ is the step function. Figure 4b shows the values of local net radiation flux predicted when parallel rays are considered (dotted line). The difference between experimental values and those calculated with the assumption of parallel beams clearly indicates that residual aberrations remain after cutting off emitted rays too tilted to be considered vertical, by absorption on the screen of blackened rectangular fins already described.

Since the emitted beams can not be considered as being parallel, their angular distribution has been approximated by an empirical function whose parameters have been regressed from experimental measurements. The adopted function is

$$P(\theta_0) = \frac{2}{\pi} \frac{\tanh^{-1}(1 - P_1)}{(1 - P_1)P_2} \operatorname{sech}\left(\frac{2\theta_0 \tanh^{-1}(1 - P_1)}{\pi P_2}\right)^2 \quad (10)$$

where $P(\theta_0)$ is the probability distribution that a photon will be emitted with a $\theta_0$ polar angle (see Figure 3b), and $P_1$ and $P_2$ are parameters of the proposed empirical function. This function has the following properties: (i) it does not depend on the $\phi_0$ angle (azimuthal symmetry condition); (ii) the maximum value of this function is found at $\theta_0 = 0$, and (iii) when either $P_1$ or $P_2$ tends to zero, the function tends to the delta function, thus approaching the case of vertical parallel beams.

When considering the angular distribution of the direction of emitted rays given by Eq. 10, it is not possible to

relate $\langle q_{z_\mathrm{p}=0}(x_\mathrm{p}, y_\mathrm{p})\rangle_{A_\mathrm{g\text{-}p}}$ to $\langle q_{r_\mathrm{p}=r_\mathrm{d}}(\theta_\mathrm{p}, \phi_\mathrm{p})\rangle_\phi$ by a simple algebraic equation as it was done with parallel rays (Eq. 9). However, this relation can be obtained by means of the Monte Carlo method. The developed algorithm relating $\langle q_{z_\mathrm{p}=0}(x_\mathrm{p}, y_\mathrm{p})\rangle_{A_\mathrm{g\text{-}p}}$ to $\langle q_{r_\mathrm{p}=r_\mathrm{d}}(\theta_\mathrm{p}, \phi_\mathrm{p})\rangle_\phi$, taking into account the propagation direction dependence adopted (Eq. 10), is shown in Figure 5. A large number of photons are generated based on stochastic rules and are tracked analytically. Then the contribution of each photon to the local radiative flux at the different radiometer locations is counted. The radiative energy associated to each emitted photon is

$$E_\mathrm{ph} = \langle q_{z_\mathrm{p}=0}(x_\mathrm{p}, y_\mathrm{p})\rangle_{A_\mathrm{g\text{-}p}} \frac{A_\mathrm{g\text{-}p}}{n_\mathrm{ph}} \tag{11}$$

where $n_\mathrm{ph}$ is the total number of photons considered in the Monte Carlo algorithm.

*Photon generation:* Both the firing point on the glass plate and the direction of each photon are stochastically assigned. Since the radiation flux was assumed to be uniform over the entire glass plate, the random point from which each photon leaves the flat plate can be computed by:

$$x_{0,\mathrm{p}} = r_\mathrm{g\text{-}p} \sqrt{R_1} \cos(2\pi R_2) \tag{12}$$

$$y_{0,\mathrm{p}} = r_\mathrm{g\text{-}p} \sqrt{R_1} \sin(2\pi R_2) \tag{13}$$

$$z_{0,\mathrm{p}} = 0 \tag{14}$$

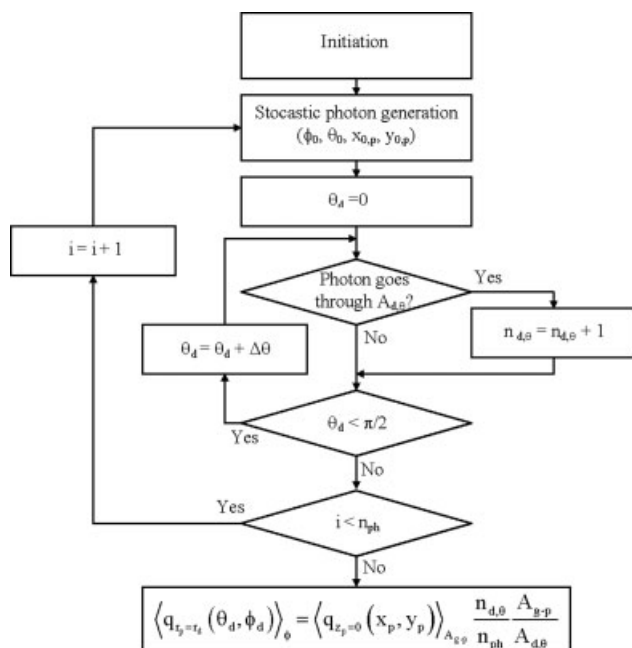where $R_1$ and $R_2$ are random numbers uniformly distributed in the interval (0,1).



**Figure 5. Monte Carlo emission/detection algorithm employed to relate $\langle q_{z_\mathrm{p}=0}(x_\mathrm{p}, y_\mathrm{p})\rangle_{A_\mathrm{g\text{-}p}}$ to $\langle q_{r_\mathrm{p}=r_\mathrm{d}}(\theta_\mathrm{d}, \phi_\mathrm{d})\rangle_\phi$.**

The direction of the outgoing photon is given by two angles:

$$\phi_0 = 2\pi R_3 \tag{15}$$

$$\theta_0 = \frac{\pi}{2} P_2 \left( \frac{\tanh^{-1}((1-P_1)R_4)}{\tanh^{-1}(1-P_1)} \right) \tag{16}$$

Note that Eq. 15 takes into account that the beam does not have a preferential $\phi_0$ angle, in accordance with the azimuthal symmetry assumption. Regarding the polar angle, note that Eq. 16 can be derived from Eq. 10 (see Appendix). Thus, each beam leaving the flat plate surface is completely characterized by its firing point $(x_{0,\mathrm{p}}, y_{0,\mathrm{p}}, z_{0,\mathrm{p}})$ and by the direction of its trajectory $(\phi_0, \theta_0)$, as it is shown in Figure 3b. Also note that, despite the problem shows rotational symmetry, the radiation propagation model is three-dimensional. On the other hand, the spectral composition of the radiation was not considered because there are not spectral properties involved so far.

*Photon counting at the radiometer location:* The photons generated according to Eqs. 12–16 may contribute to the radiative flux measured at defined positions of the detector. This spatial distribution of photons can be evaluated by tracing ray trajectories. In the current case, in which measurements are made without a monolayer of spheres over the glass plate, an emitted photon neither changes its trajectory nor is absorbed in the propagation medium (air). As a consequence of this, once the photon firing point on the glass plate $(x_{0,\mathrm{p}}, y_{0,\mathrm{p}}, y_{0,\mathrm{p}})$ and the photon initial trajectory $(\phi_0, \theta_0)$ have been assigned, its trajectory is given by

$$x_\mathrm{ph} = x_{0,\mathrm{p}} + \zeta \sin(\theta_0) \cos(\phi_0) \tag{17}$$

$$y_\mathrm{ph} = y_{0,\mathrm{p}} + \zeta \sin(\theta_0) \sin(\phi_0) \tag{18}$$

$$z_\mathrm{ph} = z_{0,\mathrm{p}} + \zeta \cos(\theta_0) \tag{19}$$

where $\zeta$ is the distance traveled by the photon in the $(\theta_0, \phi_0)$ direction. The interception point of the photons with the semisphere containing all possible locations of the detector (Figure 4a) occurs when the following condition is satisfied:

$$x_\mathrm{ph}(\zeta)^2 + y_\mathrm{ph}(\zeta)^2 + z_\mathrm{ph}(\zeta)^2 = r_\mathrm{d}^2 \Rightarrow \zeta_\mathrm{p,s} \tag{20}$$

Once this interception point has been calculated, it is possible to obtain the polar angle $\theta_\mathrm{p,s}$, referred to the main coordinate system:

$$\theta_\mathrm{p,s} = \cos^{-1}\left( \frac{z_{0,\mathrm{p}} + \zeta_\mathrm{p,s} \cos(\theta_0)}{r_\mathrm{d}} \right) \tag{21}$$

Let us call $A_{\mathrm{d},\theta}$ the detection surface generated by the rotation of the radiometer around the vertical axis at a constant $\theta_\mathrm{d}$ angle, thus generating a narrow spherical surface sector swept by $\theta_\mathrm{p}$ angles in the interval

$$abs(\theta_\mathrm{p} - \theta_\mathrm{d}) < \frac{\theta_\mathrm{va\text{-}d}}{2} \tag{22}$$

where $abs(\cdot)$ is the absolute value of the argument and $\theta_\mathrm{va\text{-}d}$ is the angle of vision of the detector from the center of the

glass plate, as depicted in Figure 4a. If the value of $\theta_{p,s}$ belongs to this interval, the interception will occur on the detection surface $A_{d,\theta}$ and the considered photon will contribute to the local radiative flux at the $\theta_d$ radiometer locations. The $\theta_{p,s}$ photon incidence angle on the detection surface is stored in individual angular counters $n_{d,\theta}$. A unit is added to the current value of $n_{d,\theta}$ whenever a photon intercepts the $A_{d,\theta}$ surface; i.e.:

$$abs\left(\theta_{p,s} - \theta_d\right) < \frac{\theta_{va\_d}}{2} \Rightarrow n_{d,\theta} = n_{d,\theta}^* + 1 \tag{23}$$

where the asterisk refers to the previous value. The flow chart of the program developed for this calculation is shown in Figure 5. Note that for every photon trajectory, the possibility of the photon reaching any of the possible detection surfaces $A_{d,\theta}$, with $\theta_d = 0°, 5°, 10°, \ldots, 85°$ is explored.

To obtain accurate results, a large number of photons were tracked ($n_{ph} = 5.0 \times 10^5$). Finally, the local net radiation flux for each $\theta_d$ angle was calculated by:

$$\left\langle q_{r_p-r_d}(\theta_d, \phi_d) \right\rangle_\phi = E_{ph} \frac{n_{d,\theta}}{A_{d,\theta}} = \left\langle q_{z_p-0}(x_p, y_p) \right\rangle_{A_{g-p}} \frac{n_{d,\theta}}{n_{ph}} \frac{A_{g-p}}{A_{d,\theta}} \tag{24}$$

The parameters $P_1$ and $P_2$ of Eqs. 10 and 16 were regressed from the experimental data using the Levenberg–Marquardt method[39] coupled to the algorithm sketched in the flow chart of Figure 5. Predicted values of $\left\langle q_{r_p=r_d}(\theta_d, \phi_d) \right\rangle_\phi$ were calculated for the set of $\theta_d$ values corresponding to experimental data processed according to Eq. 7. The optimization program minimizes the sum of the squared relative differences between predicted and experimental values. The optimized values of the parameters of Eqs. 10 and 16 are:

$$P_1 = 3.27 \times 10^{-8}; \qquad P_2 = 0.831 \tag{25}$$

In Figure 4b, predicted (solid line) and experimental ($\diamond$) values of the averaged local net radiation flux are plotted against the $\theta_d$ angle. A satisfactory agreement is observed. Besides obtaining the $P_1$ and $P_2$ parameters, this subsection allowed us to validate two submodels (the photon generation submodel and the photon counting criterion) that will be used in the following sections.

### Bead monolayer simulation

The simulation of the interaction between radiative energy and a structured heterogeneous catalytic bed needs for the description of the spatial structure of the bed. This is so even in our simpler, two-dimensional problem, because the events taking place after a beam encounters one particular bead will depend on the likely interactions with the packing surrounding that bead. The radiation beams transmitted through, or reflected on, the considered sphere may be intercepted by the neighboring ones (Figure 2). In this interaction mechanism, the relative location among the spheres is important. Therefore, the radiation model for estimating the optical properties of the fused-silica spheres of the monolayer needs for the

simulation of each monolayer spread at random on the circular glass plate.

Monolayers of randomly distributed spheres with different degrees of surface coverage were generated with a rather simple algorithm, which yields the coordinates of the bead centers. The position of each sphere in the monolayer must comply with the following constraints: (i) the position of each sphere must be randomly assigned; (ii) the distance between each one of the spheres and any other in the layer must be larger than one sphere diameter, thus excluding the possibility of sphere overlapping; and (iii) the distance between the center of the circular glass plate and the center of each sphere must be, at most, one sphere radius smaller than the plate radius (i.e., all the spheres must be contained in the circular plate).

The flow chart corresponding to the algorithm for the generation of the random monolayer is shown in Figure 6. In the first part of this algorithm, the initial spheres locations are randomly defined, whereas in the second part, the sphere locations are modified to comply simultaneously with (i)–(iii) constraints.

*Random generation of the preliminary sphere positions:* The initial location of each sphere is randomly assigned by
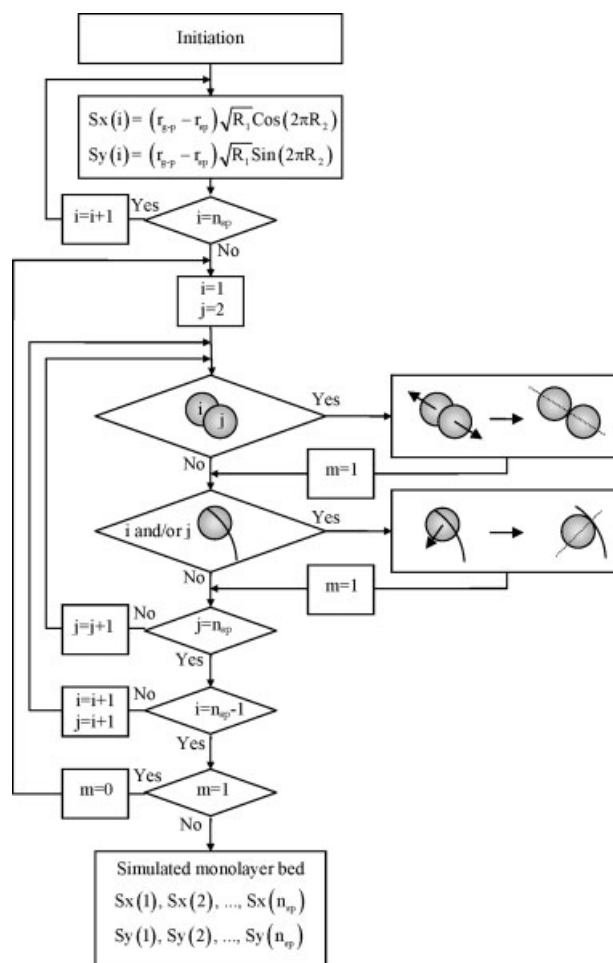


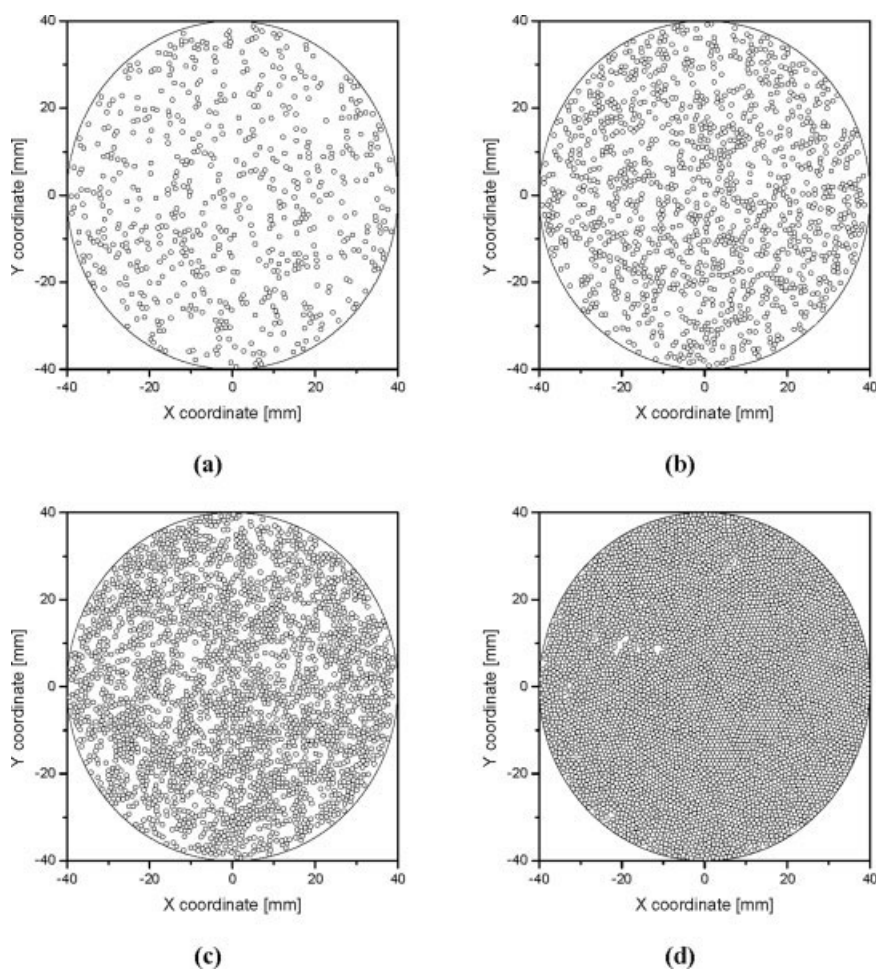**Figure 6. Algorithm developed to simulate monolayer beds of spheres.**

**Figure 7. Simulation results of the monolayer beds of spheres.**

(a) $\eta_{\text{g-p}} = 10\%$ ($\sim$640 spheres), (b) $\eta_{\text{g-p}} = 20\%$ ($\sim$1280 spheres), (c) $\eta_{\text{g-p}} = 40\%$ ($\sim$2560 spheres), (d) $\eta_{\text{g-p}} = 80\%$ ($\sim$5120 spheres).

using two random numbers, according to the following stochastic equations:

$$Sx(i) = (r_{\text{g-p}} - r_{\text{sp}})\sqrt{R_1}\,\cos(2\pi R_2); \quad i = 1, 2, \ldots, n_{\text{sp}} \quad (26)$$

$$Sy(i) = (r_{\text{g-p}} - r_{\text{sp}})\sqrt{R_1}\,\sin(2\pi R_2); \quad i = 1, 2, \ldots, n_{\text{sp}} \quad (27)$$

where $Sx(i)$ and $Sy(i)$ are the Cartesian coordinates of the $i$th sphere, and $R_1$ and $R_2$ are uniformly distributed random numbers. By using Eqs. 26 and 27, the tentative location of each one of the spheres ($i = 1, 2, \ldots, n_{\text{sp}}$) is assigned. Although the sphere locations obtained from Eqs. 26 and 27 are in agreement with conditions (i) and (iii), this preliminary sphere distribution will seldom satisfy the exclusion constraint expressed by condition (ii).

*Relocation process:* In this stage, the algorithm checks whether spheres i and j are more than one-sphere diameter apart or not. As it is shown in the algorithm flow chart of Figure 6, all possible pair combinations between $i = 1$, $2, \ldots, n_{\text{sp}} - 1$ and $j = i + 1, i + 2, \ldots, n_{\text{sp}}$ of the initial bead distribution are considered. If an $(i - j)$ pair is found such that the spheres are at less than one diameter distance

from each other, their respective locations are shifted apart along their line of centers until they ceased to overlap. Besides, when the distance between any of the spheres and the center of the circular glass plate is longer than $r_{\text{g-p}} - r_{\text{sp}}$, that bead center is outside the circular plate. In this case, the sphere is moved towards the center of the circular plate, until it crosses its boundary.

As it is shown in Figure 6, all possible combinations of $i$- and $j$-spheres are considered in the algorithm to check the compliance with conditions (i)–(iii). However, as a consequence of these location changes, another failure to comply with conditions (ii) and (iii) may arise involving different pairs of beads, which will be corrected by the recursive application of the same procedure. This relocation process is repeated until a distribution without bead overlapping or bead crossing over the plate circular boundaries is found.

The spheres in the monolayer will share the same value of their center $z$ coordinate, this common value being:

$$Sz(i) = r_{\text{sp}}; \quad i = 1, 2, \ldots, n_{\text{sp}} \quad (28)$$

Figure 7 shows the monolayers of spheres distributed at random with the algorithm just described, for different

coverage degrees of the glass plate surface. As expected, a triangular pattern appears when large values of $\eta_{g\text{-}p}$ are considered. This compact pattern is a consequence of the larger number of spheres that have to be relocated on the glass plate as the surface coverage degree increases. A similar type of pattern was experimentally observed in the actual, nonsimulated monolayers used in the experimental runs with the UV-RETM apparatus.

### Interaction between radiation and bare fused-silica spherical beads

The rather complex series of events that take place when a monolayer of fused-silica spheres of 0.1 cm average diameter is irradiated (Figure 2) was simulated by means of the Monte Carlo method, using the optical properties as probability distribution functions. The location of each sphere in the monolayer was assigned by using the previously described algorithm. The radiation source was simulated with the aid of the beam emission submodel of vertically-oriented rays. We have assumed that neither fused-silica nor air absorb radiation in the range of emission of the lamp, and that the events affecting the beam propagation obey geometric optics laws.

Regarding the reflection and the refraction of the beams on the sphere surface, there are some alternatives to model it.[40–43] The reflection/refraction phenomena at the fused-silica/air interface will be completely determined by the optical properties of the media at each side of that interface (i.e., air and fused-silica) and by the roughness degree of that interface. When the surface is smooth, the specular reflection-and-refraction model can be applied (Figure 8a). On the other extreme, when a completely rough surface is considered, in which the interface shows a high roughness degree, an isotropic reflection-and-refraction model (Figure 8b) may describe the prevailing physical situation more accurately (Lambert model). Between these two extreme situations, other models should be adopted (Figure 8c).

The optical characteristics of the fused-silica spheres surface in terms of its roughness degree is unknown. To consider the effect of the surface roughness on the reflection/refraction mechanism, the assumption that surface of the spheres can be simulated by means of the micro-facet slope method[40–43] was made. Accordingly, one micro-facet for every incoming photon is generated by using a Gaussian slope distribution:

$$P(\tau) = \frac{\exp\left(-\frac{\tau^2}{2\sigma_0^2}\right)}{\sqrt{2\pi}\sigma_0} \tag{29}$$

where $\tau$ is the tangent of the angle $(\theta_{1-n})$ between the outwardly directed normal to the spherical surface ($\mathbf{n}_{sp}$) and the outwardly directed normal to the local micro-facet ($\mathbf{n}_{loc}$), shown in Figure 8d, and $\sigma_0$ is the variance of the distribution. It is important to highlight that this method can be applied to the three earlier mentioned cases by changing the value of $\sigma_0$. Numerical values of $\sigma_0$ close to cero mean that the surface optically behaves as a plane interface, whereas larger ($\sigma_0$) values are associated with surfaces increasingly rough. When considering the micro-facet slope method, the laws of classical optics are used to describe the phenomena occurring at the point where a beam reaches the sphere
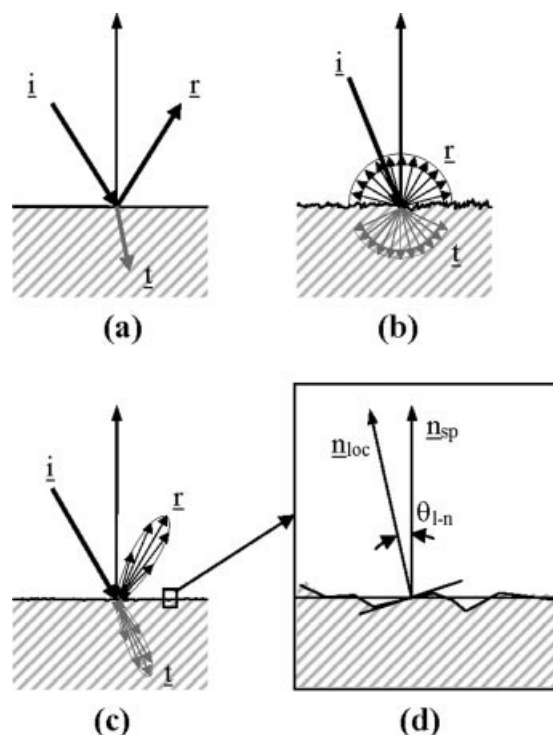


**Figure 8.** (a) Specular reflection/refraction at a plane interface; (b) diffuse reflection/refraction in a rough surface (Lambert model); (c) specular reflection/refraction at a Gaussian rough surface; (d) surface representation according the micro-facet slope method.

surface. Accordingly, the reflectivity on the micro-facet can be calculated by using Fresnel equation; the reflection law is valid on the micro facet, and Snell refraction law also holds. The beam reflection/refraction at the interface is referred to the unit vector normal to the local micro-facet ($\mathbf{n}_{loc}$) instead of the unit vector normal to the spherical surface ($\mathbf{n}_{sp}$), as sketched in Figure 8d. Therefore, the reflectivity on the micro-facet with outwardly directed normal $\mathbf{n}_{loc}$ is given by Fresnel law:

$$\rho(\mathbf{i}, \mathbf{t}, \mathbf{n}_{loc}) = \frac{1}{2}\left[\frac{n_1(\mathbf{n}_{loc} \cdot \mathbf{i}) - n_2(\mathbf{n}_{loc} \cdot \mathbf{t})}{n_1(\mathbf{n}_{loc} \cdot \mathbf{i}) + n_2(\mathbf{n}_{loc} \cdot \mathbf{t})}\right]^2$$
$$+ \frac{1}{2}\left[\frac{n_1(\mathbf{n}_{loc} \cdot \mathbf{t}) - n_2(\mathbf{n}_{loc} \cdot \mathbf{i})}{n_1(\mathbf{n}_{loc} \cdot \mathbf{t}) + n_2(\mathbf{n}_{loc} \cdot \mathbf{i})}\right]^2 \tag{30}$$

where $n_1$ and $n_2$ are the refraction index of the media at each side of the micro-facet, assuming that the beam impacts the micro-facet from medium 1, and is eventually refracted into medium 2 (see Figure 2, events 1–3–4 and 5–6–7).

The direction of the beam reflected on the micro-facet is given by the unit vector $\mathbf{r}$, which is related to the unit vector $\mathbf{i}$ (pointing in the direction opposite to that of the incident beam), through the vector form of the reflection equation:

$$\mathbf{n}_{loc} \times \mathbf{i} = (\mathbf{n}_{loc} \times \mathbf{r}); \quad \mathbf{r} \neq \mathbf{i} \tag{31}$$
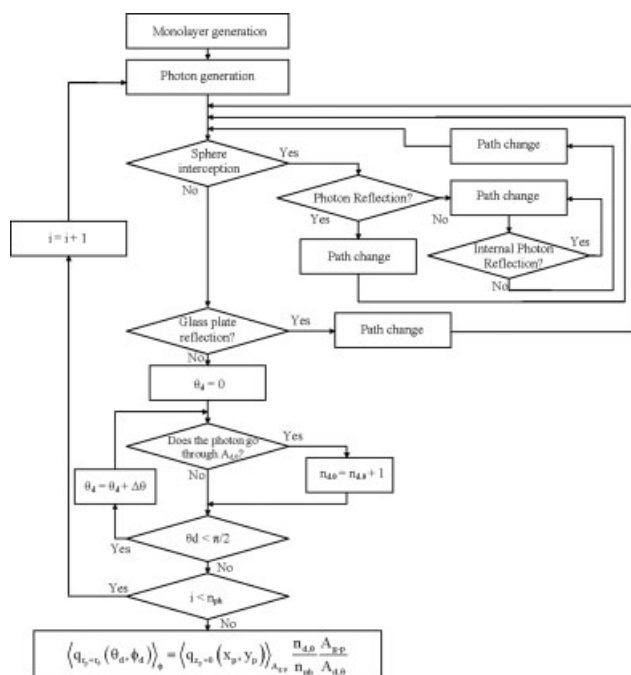
**Figure 9. Monte Carlo algorithm employed to simulate the interaction between radiation and uncoated spheres.**

Similarly, the direction of the transmitted beam is given by the unit vector $\mathbf{t}$, which is the solution of the vector form of Snell equation:

$$\mathbf{n}_{loc} \times \mathbf{i} = \frac{n_2}{n_1}(\mathbf{n}_{loc} \times \mathbf{t}); \quad \mathbf{t} \neq \mathbf{i}\,\frac{n_1}{n_2} \qquad (32)$$

Taking advantage of the Monte Carlo method allows us to combine individual computational modules, such as: (i) the radiation emission and the sphere monolayer modules; (ii) the photon counting procedure; and (iii) the solution module of the reflection equation, and those of the Snell and Fresnel equations for the micro-facet rough-surface model. The flow chart of the complete Monte Carlo algorithm developed to solve this problem is shown in Figure 9. Details of this algorithm are presented in the following paragraphs.

*Monolayer generation:* As it was described in the previous subsection, the position of each sphere on the glass plate was randomly assigned by a computer program to simulate the actual monolayer used in the experiments. The numerical values of the coordinates corresponding to the location of each sphere are kept in storage for further use in this algorithm.

*Photon generation:* The photon generation submodel previously described was used. The point from which each photon leaves the flat glass plate and its initial direction were generated at random, according to Eqs. 12–16. Then, they were tracked analytically (Eqs. 17–19) to determine their interaction with the spheres in the monolayer.

*Sphere interception:* The possible interaction between a photon and each sphere in the monolayer is considered. The minimum distance from the photon trajectory to a given sphere center is calculated. If this distance is larger than one

sphere radius, there is no interaction between the considered sphere and the photon, and the next candidate sphere is considered. This procedure is repeated until all the spheres has been considered ($i = 1, 2, \ldots, n_{sp}$). If more than one sphere are intercepted, only the interaction with the nearest one is retained. The interception point between the nearest sphere and the photon can be easily calculated by applying geometric optics. The unit vector normal to the spherical surface at the point of interception can be obtained as follows:

$$\mathbf{n}_{sp} = \frac{\mathbf{n}_{int} - \mathbf{S}}{r_{sp}} \qquad (33)$$

where $\mathbf{S} = [Sx(i), Sy(i), Sz(i)]$ is the position vector of the center of the nearest intercepted sphere and $\mathbf{n}_{int}$ is the point where the photon intercepts the surface of that sphere.

*Rough surface modeling:* The sphere surface was considered to have an unknown degree of roughness. According to the micro-facet method, the direction $(\theta_{1-n}, \phi_{1-n})$ of the normal to the local micro-facet with respect to the normal to the sphere ($\mathbf{n}_{sp}$) can be randomly assigned:

$$\phi_{1-n} = \pi R_1 \qquad (34)$$

$$\theta_{1-n} = \tan^{-1}(\sqrt{2}\,\sigma_0\,\mathrm{erf}^{-1}(R_2)) \qquad (35)$$

where $\mathrm{erf}^{-1}(\cdot)$ is the inverse error function. By solving the system of Eqs. 33–35 the $\mathbf{n}_{loc}$ unit vector can be obtained. Then, with Eqs. 30–32 it is possible to compute $\mathbf{r}$, $\mathbf{t}$, and $\rho(\mathbf{i}, \mathbf{n}_{loc})$, which are required in the next computation step.

*Photon reflection/refraction:* The photon reflection/refraction on a fused-silica micro-facet is simulated by comparing the local reflectivity $\rho(\mathbf{i}, \mathbf{n}_{loc})$ with a random number $R_3$. If $R_3 < \rho(\mathbf{i}, \mathbf{n}_{loc})$, the photon is reflected in the $\mathbf{r}$ direction according to Eq. 31 (also see case 3 of Figure 2), otherwise the photon is refracted in the t direction according to Eq. 32 (also see case 4 of Figure 2). The trajectory of a reflected or refracted photon is tracked, so that the next interception point (either it be an air/fused-silica interface or a fused-silica/air interface) can be defined. Again, the rough surface model is applied, and the probability of the photon being reflected or refracted is assessed as before. Throughout this process, the multiple reflections and refractions that a photon may undergo before leaving the monolayer are taken into account, as depicted in Figure 2.

*Glass plate interception:* In their trajectories, some photons may reach back the glass plate from which they departed. In such case, the photon can be reflected on the glass and returned to the bead monolayer. Then, only reflected photons are subsequently considered, and those photons that are refracted by the glass plate are disregarded. When calculating the reflectivity for this event through Eq. 30, the refraction index of the borosilicate glass is employed ($n_{g-p} = 1.514$).

*Photon counting at the radiometer location:* Once the trajectories of the rays leaving the monolayer of beads have been determined, the point of interception of photons with the semisphere containing all possible locations of the detector are known (see Eqs. 17–21). To count the number of photons reaching the radiometer location, the criterion previously described is applied. The polar angle of the points of

**Table 1. Model Parameters Values Obtained from Experimental Measurements**

| Parameter | Value | 95% Confidence Interval |
|---|---|---|
| $n_{\text{f-s}}$ | 1.537 | ±0.007 |
| $\sigma_{0,\text{f-s}}$ | ~0 | – |
| $n_{\text{f-s/TiO}_2}$ | 1.520 | ±0.017 |
| $e_{\text{TiO}_2}$ | 4.45 | ±0.14 |
| $\sigma_{0,\text{f-s/TiO}_2}$ | ~0 | – |

interception of photons with the semisphere containing all possible locations of the detector in the main coordinate system ($\theta_s$) is used to establish whether the photon energy is collected or not by the detector placed at a given angle ($\theta_d$), according to Eq. 23. Finally, the $\langle q_{r_p = r_d}(\theta_d, \phi_d) \rangle_\phi$ values are obtained on the basis of the photon detection criterion previously described (Eq. 24).

The unknown parameters $n_{\text{f-s}}$ and $\sigma_0$ were determined from the experimental data by using the algorithm shown in Figure 9 and the Levenberg–Marquardt optimizer. The numerical values of $n_{\text{f-s}}$ and $\sigma_{0,\text{f-s}}$ are expected to be positive numbers because of their physical meaning. This constraint was incorporated to the Levenberg–Marquardt optimizer.[39] Table 1 shows the best fit values of these parameters. Notice that the optimization algorithm predicts a zero value for $\sigma_{0,\text{f-s}}$. This result means that the fused-silica surface is optically smooth, and it can be modeled as shown in Figure 8a. Experimental values of the local net radiation flux and the corresponding model predictions against the $\theta_d$ angle are shown in Figure 10. Each group of values corresponds to different degrees of coverage of the plate surface with uncoated spheres. The average relative error between experimental and predicted values is 17.8%. Considering that the direction of a beam is deflected from its initial vertically-oriented direction when a sphere is intercepted, the local net radiation flux at larger $\theta_d$ angles increases with the surface coverage as a consequence of increasing the number of intercepted spheres per unit area. The opposite trend is observed for small $\theta_d$ angles: more photons with trajectories around the vertical will be detected as the number of spheres in the monolayer decreases, thus diminishing the interactions between beams and spheres and leaving a larger interstitial area.

### Interaction between radiation and TiO₂-coated fused-silica spherical beads

To complete the set of the properties required to model the interaction between the radiation field and a photocatalytic packed bed made of TiO₂-coated spheres, it is necessary knowing the optical thickness of the TiO₂ film, as well as the refraction index of the fused-silica/TiO₂ composite. For this, experiments have been carried out with the same experimental setup, but spreading randomly TiO₂-coated spheres on the glass plate instead of bare fused-silica spheres, as we did before. Although the assumptions made in the previous subsection for the case of a monolayer of bare fused-silica beads also hold for TiO₂-coated spheres, in this case we have to take into account the spectral nature of the radiation. The model of the interaction between radiation and TiO₂-coated fused-silica spheres has to account for the fact that

energy absorption in the TiO₂ films is a wavelength dependent phenomenon. We also assume that the transmittance of the TiO₂ films is independent of the angle of incidence of the photon.

To model the system considered, the algorithm shown in Figure 9 was employed, except for the fact that the effect of the TiO₂ film thickness on the radiation field was taken into account. In this way, the procedures previously used to model the monolayer, the photon generation, the photon interceptions by the spheres or the glass plate, and the photon counting at the radiometer location are applied in this case. It was necessary to incorporate only three changes to the basic algorithm shown in Figure 9:

*Photon generation:* As before, the origin and the initial direction of photons were defined by means of Eqs. 12–16. However, it was necessary to incorporate the spectral nature of the photons. For this reason, the wavelength of the emitted photon was assigned based on the spectral emission of the lamp (see Appendix). Thus, each photon leaving the flat plate is characterized by its firing point ($x_{0,p}$, $y_{0,p}$, $y_{0,p}$), by the direction of its trajectory ($\phi_0$, $\theta_0$), and by its wavelength ($\lambda$).

*Photon reflection/refraction:* This event has been modeled as we did for the case of bare beads, but considering the refraction index of the composite of fused-silica and TiO₂ coating ($n_{\text{f-;s/TiO}_2}$) to evaluate the reflectivity by means of the Fresnel law (Eq. 30). However, the direction of propagation of the refracted photons are given by Snell law considering both the refraction index of the air phase and that of the fused-silica phase.

*Photon energy absorption:* In the case of the interaction between the radiation field and a monolayer of uncovered fused-silica beads, the energy of a photon remains invariant along its trajectory from the point of generation until it leaves the monolayer. During its travel, a photon may change its direction as a consequence of its reflection or refraction on the solid-fluid interfaces, but it will not change its energy. In the case of fused-silica beads coated with thin TiO₂ films, the wavelength-dependent absorption of the beam energy by the thin TiO₂ films has to be taken into account. Under such
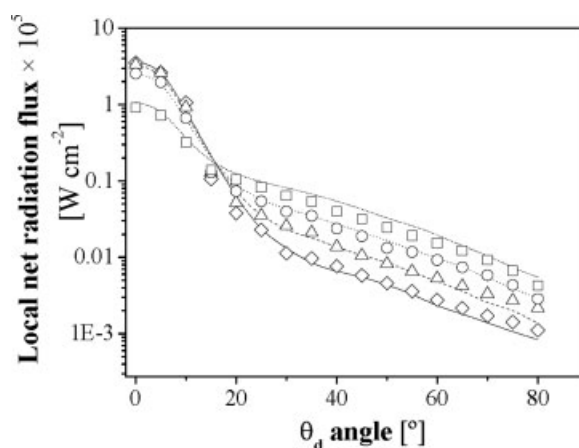


**Figure 10. Experimental and predicted values of local net radiation flux for uncoated spheres.**

Keys: (◇) $\eta_{\text{g-p}}$ = 10% (~640 spheres), (△) $\eta_{\text{g-p}}$ = 20% (~1280 spheres), (○) $\eta_{\text{g-p}}$ = 40% (~2560 spheres), (□) $\eta_{\text{g-p}}$ = 80% (~5120 spheres).

conditions, when a beam comprised of photons of different wavelengths crosses a TiO$_2$ film, the radiative energy it carries is partially absorbed in different degrees depending on the fraction of photons of each wavelength and of the wavelength dependence of the film transmittance. Because of the experimental difficulty of measuring the spectral transmittance of TiO$_2$ films deposited on fused-silica spheres, the optical properties of the TiO$_2$ films were adopted from published data. In a previous work,[24] the optical properties of TiO$_2$ films immobilized over a borosilicate glass flat plate were obtained. These films were prepared by using the same sol–gel technique that we have used in this work. The wavelength dependence of the transmittance of these films has been adopted in the present work. However, the optical thickness of the film on the glass plate not necessarily will be equal to that of the film on the spheres, but the relative optical thickness is easy to obtain from our experimental measurements.

Taking into account the attenuation effects in the TiO$_2$ films, the energy associated to each photon beam is

$$E_{\mathrm{ph}} = \langle q_{z_{\mathrm{p}}=0}(x_{\mathrm{p}}, y_{\mathrm{p}}) \rangle_{A_{\mathrm{g\text{-}p}}} \frac{A_{\mathrm{g\text{-}p}}}{n_{\mathrm{ph}}} \{1 - \exp[-e_{\mathrm{TiO_2}} \kappa_{\mathrm{TiO_2}}(\lambda)]\}^{n_i}$$

$$(36)$$

where $n_i$ is the number of times that the $i$th photon crosses a TiO$_2$ film, $\kappa_{\mathrm{TiO_2}}(\lambda)$ is the reference spectral absorbance of a previously characterized TiO$_2$ film, and $e_{\mathrm{TiO_2}}$ is the optical thickness of the TiO$_2$ films relative to the reference spectral values.

As it was done previously, the algorithm shown in Figure 9, with the three mentioned changes, was coupled with a Levenberg–Marquardt method[39] to obtain the optical properties of the TiO$_2$ films from the experimental measurements. Table 1 shows the numerical values obtained of the relative optical thickness and the refractive index of the composite of fused-silica and TiO$_2$ coating. Again, the predicted value of $\sigma_{0,\mathrm{f\text{-}s/TiO_2}}$ is zero. Therefore, the TiO$_2$-coated surfaces are optically smooth. Experimental values and model predictions of the local net radiation flux against $\theta_{\mathrm{d}}$ are shown in Figure 11, where the average relative error is 10.7%. All values correspond to the same degree of plate surface coverage either by TiO$_2$-coated or uncoated spheres: $\eta_{\mathrm{g\text{-}p}} = 80\%$ (~5120 spheres). The local net radiation flux for small $\theta_{\mathrm{d}}$ angles primarily depends on the interstitial area and is independent on whether the beads are coated or uncoated. The beams detected at larger $\theta_{\mathrm{d}}$ angles have been deflected from their original, vertically-oriented trajectories because of their interaction with one or more beads. This is the reason why at larger $\theta_{\mathrm{d}}$ angles the difference between the local net radiation flux for coated and uncoated spheres becomes apparent. In this region, the curve representing the local net radiation flux for TiO$_2$-coated spheres lies below the one for uncovered beads due to the energy absorption by the TiO$_2$ coating. The agreement between Monte Carlo simulations and experimental results is satisfactory.

## Conclusions

A detailed Monte Carlo model was developed to simulate the complex interaction between radiation and monolayers of
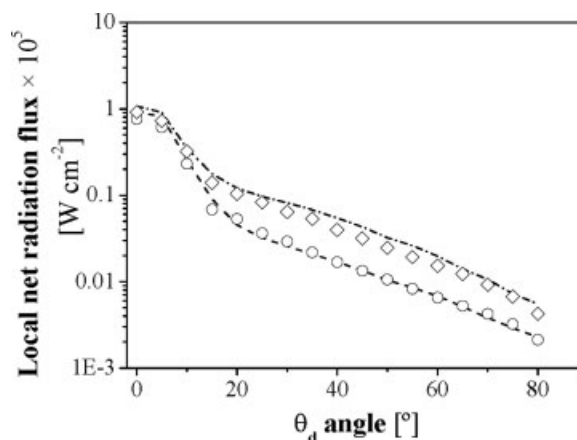


**Figure 11. Experimental and predicted values of local net radiation flux ($\eta_{\mathrm{g\text{-}p}}$ = 80%, ⌣5120 spheres).**

Keys: (◇) uncoated fused-silica spheres, (○) TiO$_2$-coated fused-silica spheres.

spheres. The optical properties of bare fused-silica spheres and those of TiO$_2$-coated, fused-silica spheres were obtained. An ad hoc experimental setup was developed to measure the spatial distribution of the net radiation flux resulting from the interaction of normal-oriented UV radiation and the monolayers of spheres. By means of different computational algorithms, the required optical properties were obtained from the experimental data. These optical properties include: (i) the refractive index and the surface rough index of the bare fused-silica spheres; (ii) the refractive index of the fused-silica/TiO$_2$ coating composite; (iii) its surface rough index; and (iv) the optical thickness of the TiO$_2$ films. Besides, the model to predict the interaction between the spheres and radiation has been experimentally validated.

This is the first step of a methodology leading to the final objective of modeling and simulating the radiation field in a structured (i.e., nonhomogeneous) annular fixed bed photocatalytic reactor. The developed algorithm will be used to solve the fixed bead reactor by changing the sphere pattern (i.e., using an annular multilayer of packed spheres instead a single monolayer).

## Notation

$A$ = area, cm$^2$
$e$ = relative optical thickness, dimensionless
$E$ = radiative energy associated to a given photon, W
$H(\cdot)$ = step function, dimensionless
$I$ = specific radiation intensity, W cm$^{-2}$ sr$^{-1}$
$\mathbf{i}$ = incidence unit vector, dimensionless
$n$ = reflection index relative to air, dimensionless
$\mathbf{n}_{\mathrm{gp}}$ = unit vector normal to the glass plate, dimensionless

$\mathbf{n}_{loc}$ = local outwardly directed unit vector normal to the rough surface, dimensionless

$n_m$ = number of experimental measurements taken into account to obtain an average value

$n_{ph}$ = total number of photons

$\mathbf{n}_{sp}$ = outwardly directed unit vector normal to the sphere surface, dimensionless

$n_{sp}$ = total number of spheres

$P$ = probability distribution function, dimensionless

$P_1, P_2$ = parameters defined in Eq. 10, dimensionless

$q$ = local net radiation flux, W cm$^{-2}$

$r$ = radius, cm

$\mathbf{r}$ = reflection unit vector, dimensionless

$R$ = uniformly distributed random number, dimensionless

$r_0$ = radial coordinate in the auxiliary spherical coordinate system, cm

$r_p$ = radial coordinate in the main spherical coordinate system, cm

$\mathbf{S}$ = position vector of a spherical bead center, cm

$Sx$ = $x$ coordinate of a spherical bead center, cm

$Sy$ = $y$ coordinate of a spherical bead center, cm

$Sz$ = $z$ coordinate of a spherical bead center, cm

$\mathbf{t}$ = transmission unit vector, dimensionless

$x_{0,p}$ = rectangular coordinate in the auxiliary coordinate system, cm

$x_p$ = rectangular coordinate in the main coordinate system, cm

$y_{0,p}$ = rectangular coordinate in the auxiliary coordinate system, cm

$y_p$ = rectangular coordinate in the main coordinate system, cm

$z_{0,p}$ = rectangular coordinate in the auxiliary coordinate system, cm

$z_p$ = rectangular coordinate in the main coordinate system, cm

### Greek letters

$\delta$ = Dirac delta function, dimensionless

$\zeta$ = distance traveled by the photon, cm

$\eta_{g-p}$ = surface coverage degree of the glass plate, dimensionless

$\theta_0$ = polar angle in the auxiliary spherical coordinate system, rad

$\theta_p$ = angle in the auxiliary spherical coordinate system, rad

$\theta_{va-d}$ = view angle of the detector from the center of the glass plate, rad

$\kappa$ = spectral absorption coefficient, dimensionless

$\lambda$ = wavelength, nm

$\sigma_0$ = variance of the distribution of slopes on a rough surface, dimensionless

$\tau$ = tangent of the angle $\theta_{1-n}$ defined in Figure 8d, dimensionless

$\phi_0$ = Azimuthal angle in the auxiliary spherical coordinate system, rad

$\phi_p$ = Azimuthal angle in the main spherical coordinate system, rad

$\Omega$ = solid angle, sr

$\mathbf{\Omega}$ = unit vector in the direction of propagation of a beam, dimensionless

### Subscripts

$\lambda$ = denotes wavelength

$A_{g-p}$ = relative to the area of the glass plate

d = relative to the UV detector

exp = relative to experimental results

f = relative to the TiO$_2$ film

f-s = relative to the fused-silica

g-p = relative to the glass plate

loc = relative to the local value

m = relative to the measurements

max = relative to the maximum value

min = relative to the minimum value

n = normal to a given surface

va-d = relative to the vision angle of the center of the glass plate from the detector

sp = relative to the fused-silica spheres

p-r = relative to the parallel rays assumption

ph = relative to the photons

TiO$_2$ = relative to the TiO$_2$ films

### Superscripts

* = relative to the previous value in an iterative process

### Special symbols

$\langle \cdot \rangle$ = means average value over a given interval

## Literature Cited

1. Hoffman MR, Martin ST, Choi W, Bahnemann DW. Environmental applications of semiconductor photocatalysis. *Chem Rev*. 1995; 95:69–96.
2. Fujishima A, Rao TN, Tryk DA. Titanium dioxide photocatalysis. *J Photoch Photobio C*. 2000;1:1–21.
3. Blake DM. *Bibliography of Work on the Heterogeneous Photocatalytic Removal of Hazardous Compounds from Water and Air 2001*. Golden, Colorado: National Renewable Energy Laboratory, 2001.
4. Peral J, Domènech X, Ollis DF. Heterogeneous photocatalysis for purification, decontamination and deodorization of air. *J Technol Biotechnol*. 1997;70:117–140.
5. Zhao J, Yang X. Photocatalytic oxidation for indoor air purification: a literature review. *Build Environ*. 2003;38:645–654.
6. De Lasa H, Serrano B, Salaices M. *Photocatalytic Reaction Engineering*. New York: Springer, 2005.
7. Herrmann JM. Heterogeneous photocatalysis: fundamentals and applications to the removal of various types of aqueous pollutants. *Catal Today*. 1999;53:115–129.
8. Bahnemann D. Photocatalytic water treatment: solar energy applications. *Sol Energy*. 2004;77:445–459.
9. Cassano AE, Martín CA, Brandi RJ, Alfano OM. Photoreactor analysis and design: fundamentals and applications. *Ind Eng Chem Res*. 1995;34:2155–2201.
10. Nicolella C, Rovatti M. Mathematical modelling of monolith reactors for photocatalytic oxidation of air contaminants. *Chem Eng J*. 1998;69:119–126.
11. Hall RJ, Bendfeldt P, Obee TN, Sangiovanni JJ. Computational and experimental studies of UV/titania photocatalytic oxidation of VOCs in honeycomb monoliths. *J Adv Oxid Technol*. 1998;3:243–252.
12. Hossain MM, Raupp GB. Polichromatic radiation field model for a honeycomb monolith photoreactor. *Chem Eng Sci*. 1999;54:3027–3034.
13. Raupp GB, Alexiadis A, Hossain M, Changrani R. First-principles modeling, scaling laws and design of structured photocatalytic oxidation reactors for air purification. *Catal Today*. 2001;69:41–49.
14. Hossain MM, Raupp GB. Radiation field modeling in a photocatalytic monolith reactor. *Chem Eng Sci*. 1998;53:3771–3780.
15. Avila P, Sánchez B, Cardona AI, Rebollar M, Candal R. Influence of the methods of TiO$_2$ incorporation in monolithic catalysts for the photocatalytic destruction of chlorinated hydrocarbons in gas phase. *Catal Today*. 2002;76:271–278.
16. Alexiadis A. 2-D radiation field in photocatalytic channels of square, rectangular, equilateral triangular and isosceles triangular sections. *Chem Eng Sci*. 2006;61:516–525.
17. Esterkin CR, Negro AC, Alfano OM, Cassano AE. Radiation field inside a reactor of glass-fiber meshes coated with TiO$_2$. *AIChE J*. 2002;48:832–845.
18. Changrani R, Raupp GB. Monte Carlo simulation of the radiation field in a reticulated foam photocatalytic reactor. *AIChE J*. 1999; 45:1085–1094.
19. Changrani R, Raupp GB. Two-dimensional heterogeneous model for a reticulated-foam photocatalytic reactor. *AIChE J*. 2000;46:829–842.
20. Shang H, Zhang Z, Anderson WA. Nonuniform radiation modeling of a corrugated plate photocatalytic reactor. *AIChE J*. 2005;51:2024–2033.
21. Zhang Z, Anderson WA, Moo-Young M. Rigorous modeling of UV absorption by TiO$_2$ in a photocatalytic reactor. *AIChE J*. 2000; 46:1461–1470.
22. Zhang Z, Anderson WA, Moo-Young M. Modeling of corrugated plate photocatalytic reactors and experimental validation. *Chem Eng Sci*. 2003;58:911–914.
23. Imoberdorf GE, Irazoqui HA, Cassano AE, Alfano OM. Photocatalytic degradation of tetrachloroethylene in gas phase on TiO$_2$ films: a kinetic study. *Ind Chem Eng Res*. 2005;44:6075–6085.
24. Imoberdorf GE, Cassano AE, Irazoqui HA, Alfano OM. Optimal design and modeling of annular photocatalytic wall reactors. *Catal Today*. doi: 10.1016/j.cattod.2107.06.057.

25. Imberdorf GE, Irazoqui HA, Cassano AE, Alfano OM. Modeling of a multi-annular photocatalytic reactor for PCE degradation in air. *AIChE J*. 2006;52:1814–1823.
26. Imberdorf GE, Cassano AE, Irazoqui HA, Alfano OM. Simulation of a multi-annular photocatalytic reactor for degradation of perchloroethylene in air. Parametric analysis of radiative energy efficiencies. *Chem Eng Sci*. 2007;62:1138–1154.
27. Raupp GB, Nico JA, Annangi S, Changrani R, Annapragada R. Two-flux radiation model for an annular packed-bed photocatalytic oxidation reactor. *AIChE J*. 1997;43:792–801.
28. Imberdorf GE, Irazoqui HA, Alfano OM, Cassano AE. Scaling-up from first principles of a photocatalytic reactor for air pollution remediation. *Chem Eng Sci*. 2007;62:793–804.
29. Irazoqui HA, Isla MA, Brandi RJ, Cassano AE. Packed-bed photocatalytic reactors. A packing structure model and its experimental validation with computerized tomography. *Ind Eng Chem Res*. 2004;43:1430–1442.
30. Spadoni G, Bandini E, Santarelli F. Scattering effects in photosensitized reactions. *Chem Eng Sci*. 1978;33:517–524.
31. Pasqualli M, Santarelli F, Porter JF, Yue PL. Radiative transfer in photocatalytic systems. *AIChE J*. 1996;42:532–537.
32. Yang QY, Ang PL, Ray MB, Pehkonen SO. Light distribution field in catalyst suspensions within an annular photoreactor. *Chem Eng Sci*. 2005;60:5255–5268.
33. Stankevich D, Shkuratov Y. Monte Carlo ray-tracing simulation of light scattering in particulate media with optically contrast structure. *J Quant Spectrosc Rad Heat Transfer*. 2004;87:289–296.
34. Singh BP, Kaviany M. Modelling radiative heat transfer in packed beds. *Int J Heat Mass Transfer*. 1992;35:1397–1405.
35. Desjardins AE. Angularly resolved backscattering of light from turbid suspensions of dielectric spheres. *J Quant Spectrosc Rad Transfer*. 2006;102:139–151.
36. Singh BP, Kaviany M. Independent theory versus direct simulation of radiation heat transfer in packed beds. *Int J Heat Mass Transfer*. 1991;34:2869–2882.
37. Jiménez J, Curcó D. Modelos cinéticos y de radiación en sistemas fotocatalíticos. In: Blesa MA, Sánchez B, editors. *Eliminación de Contaminantes por Fotocatálisis Heterogénea*. Madrid, España: CIEMAT, 2004:243–255.
38. Yamazaki-Nishida S, Nagano KJ, Phillips LA, Cervera-March S, Anderson MA. Photocatalytic degradation of trichloroethylene in the gas phase using titanium dioxide pellets. *J Photoch Photobio A*. 1993;70:95–99.
39. Press WH, Teukolsky SA, Vetterling WT, Flannery BP. *Numerical Recipes*, 2nd ed. New York: Cambridge University Press, 1996.
40. Lee HJ, Lee BJ, Zhang ZM. Modeling the radiative properties of semitransparent wafers with rough surfaces and thin-film coatings. *J Quant Spectrosc Rad Heat Transfer*. 2005;93:185–194.
41. Warnick KF, Chew WC. Numerical simulation methods for rough surface scattering. *Wave Random Media*. 2001;11:R1–R30.
42. Tang K, Buckius RO. The geometric optics approximation for reflection from two-dimensional random rough surfaces. *Int J Heat Mass Transfer*. 1998;41:2037–2047.
43. Tang K, Buckius RO. A statistical model of wave scattering from random rough surfaces. *Int J Heat Mass Transfer*. 2001;44:4059–4073.

## Appendix

The general problem we have to deal with in this appendix is that of assigning values to a random variable $\chi$ distributed over the interval $(a < \chi < b)$ with provability density $P(\chi)$. For this, we have to solve the following equation

$$P(\chi) = \int_a^\chi P_\chi(\chi')d\chi' = R; \qquad a < \chi < b \qquad (A1)$$

In Eq. A.1, $P(\chi)$ is the cumulative probability that the random variable has a value between $a$ and $\chi$, and $R$ is an evenly distributed variable (i.e., $P_R(R) = 1$) over the interval $(0,1)$.

We require that Eq. A.1 satisfies the following conditions:

$$P(a) = 0 \qquad (A2)$$

$$P(b) = 1 \qquad (A3)$$

By differentiation of Eq. A.1 with respect to the random variable $R$, we get

$$P_\chi(\chi)\frac{d\chi}{dR} = 1 \qquad (A4)$$

If $\chi$ is monotonically increasing with $R$ in the interval $(a < \chi < b)$, then we have

$$P_\chi(\chi) \geq 0 \qquad (A5)$$

The values of the random variable R are drawn out from the set of uniformly distributed random numbers.

*Definition of the direction of the emitted photon:* The emission of photons was made with the assumption of azimuthal symmetry. Therefore:

$$P(\phi_0) = \frac{1}{2\pi} \qquad (A6)$$

$$\int_0^{\phi_0} P(\phi_0)d\phi_0 = \frac{\phi_0}{2\pi} = R \qquad (A7)$$

$$\phi_0 = 2\pi R \qquad (A8)$$

The polar angle was determined by means of the empirical function:

$$P(\phi_0) = \frac{2 \, \tanh^{-1}(1 - P_1)}{\pi \, (1 - P_1)P_2} \, \mathrm{sec}h\left(\frac{2\theta_0 \, \tanh^{-1}(1 - P_1)}{\pi P_2}\right)^2 \qquad (A9)$$

$$\int_0^{\theta_0} P(\theta_0)d\theta_0 = \frac{\tanh\left(\frac{2\theta_0 \, \tanh^{-1}(1-P_1)}{\pi P_2}\right)}{(1 - P_1)} = R \qquad (A10)$$

$$\theta_0 = \frac{\pi}{2}P_2\frac{\tanh^{-1}((1 - P_1)R)}{\tanh^{-1}(1 - P_1)} \qquad (A11)$$

*Definition of the origin point of the emitted photon:* The radiation is emitted uniformly on the glass plate. Thus:

$$P(\phi_{0,\mathrm{p}}) = \frac{1}{2\pi} \Rightarrow \phi_{0,\mathrm{p}} = 2\pi R \qquad (A12)$$

$$P(r_{0,\mathrm{p}}) = \frac{2r_{0,\mathrm{p}}}{(r_{\mathrm{g-p}})^2} \Rightarrow r_{0,\mathrm{p}} = r_{\mathrm{g-p}}\sqrt{R} \qquad (A13)$$

*Definition of the initial location of each sphere on the glass plate:* The initial position of each spheres was defined

considering an uniform distribution on the circular glass plate:

$$P(\phi_0) = \frac{1}{2\pi} \Rightarrow \phi_P = 2\pi R \qquad (A14)$$

$$P(r_p) = \frac{2r_p}{(r_{g\text{-}p} - r_{sp})^2} \Rightarrow r_p = (r_{g\text{-}p} - r_{sp})\sqrt{R} \qquad (A15)$$

*Definition of the orientation of a local micro-facet respect to the normal vector of the sphere surface:* The random rough surface of the spheres was simulated by means of the micro-facet slope method, which generates one micro-facet for every incoming beam according to a slope distribution. This distribution is modeled with the following equation:

$$P(\tau) = \frac{\exp\left(-\frac{\tau^2}{2\sigma_0^2}\right)}{\sqrt{2\pi}\sigma_0} \qquad (A16)$$

By integration of the distribution function $P(\tau)$ over the range of $\tau$, we get,

$$\int_{-\infty}^{\infty} P(\tau)d\tau = \frac{1}{\sqrt{2\pi}\sigma_0} \int_{-\infty}^{\infty} \exp\left(-\frac{\tau^2}{2\sigma_0^2}\right)d\tau = 1 \qquad (A17)$$

i.e., the distribution satisfies the normalization condition. The average (or expected) value of $\tau$ is

$$\langle \tau \rangle = \int_{-\infty}^{\infty} \tau P(\tau)d\tau = \frac{1}{\sqrt{2\pi}\sigma_0} \int_{-\infty}^{\infty} \tau \exp\left(-\frac{\tau^2}{2\sigma_0^2}\right)d\tau = 0 \qquad (A18)$$

result that is consistent with the fact that the unit vector normal to the micro-facet is tilted at random around the spherical radial direction. On the other hand, the expected value of $\tau^2$ is

$$\langle \tau^2 \rangle = \int_{-\infty}^{\infty} \tau^2 P(\tau)d\tau = \frac{1}{\sqrt{2\pi}\sigma_0} \int_{-\infty}^{\infty} \tau^2 \exp\left(-\frac{\tau^2}{2\sigma_0^2}\right)d\tau = \sigma_0^2 \qquad (A19)$$

Because in this case the expected value of $\tau$ is zero, we have

$$\sigma_0^2 = \langle \tau^2 \rangle - \langle \tau \rangle^2 = \langle \tau^2 \rangle \qquad (A20)$$

The cumulative probability that $\tau'$ has a value between zero and $\tau$ is

$$P[(0 < \tau' < \tau)] = \int_{-\infty}^{\tau} P(\tau')d\tau'$$

$$= \frac{1}{\sqrt{2\pi}\sigma_0} \int_{-\infty}^{\tau} \exp\left(-\frac{\tau'^2}{2\sigma_0^2}\right)d\tau' \qquad (A21)$$

The random variable $\tau(R_1)$, with $R_1$ a random number, can be obtained by solving

$$\int_{-\infty}^{\tau(R_1)} P(\tau')d\tau' = \frac{1}{\sqrt{2\pi}\sigma_0} \int_{-\infty}^{\tau(R_1)} \exp\left(-\frac{\tau'^2}{2\sigma_0^2}\right)d\tau'$$

$$= \mathrm{erf}\left(\frac{\tau(R_1)}{\sqrt{2}\sigma_0}\right) = R_1 \qquad (A22)$$

Equation A.22 may also be written in terms of the random variable $\theta_{1-n}$

$$\mathrm{erf}\left(\frac{\tan\theta_{1-n}}{\sqrt{2}\sigma_0}\right) = R_1 \qquad (A23)$$

with $(-\pi/2 < \theta_{1-n} < \pi/2)$.

The angle $\phi_{1-n}$ is a uniformly distributed random variable in the interval $0 < \phi_{1-n} < \pi$. Therefore, its values are given by the following stochastic equation

$$\phi_{1-n} = \pi R_2 \qquad (A24)$$

where $R_2$ is a random number.

*Definition of the wavelength of the emitted photon:* It was simulated based on the spectral emission of the lamp. The spectral distribution $P(\lambda)$ is given by the lamp manufacturer. In this case, the whole range of wavelengths was discretized. Therefore, the photon wavelength must verify the following condition:

$$\begin{cases} \int_{\lambda_0}^{\lambda_i} P(\lambda)d\lambda < R \\ \int_{\lambda_0}^{\lambda_{i+1}} P(\lambda)d\lambda > R \end{cases} \Rightarrow \lambda = \lambda_{i+1} \qquad (A25)$$